

Article

Assessment of the High Resolution SAR Mode of the RADARSAT Constellation Mission for First Year Ice and Multiyear Ice Characterization

Mohammed Dabboor ^{1,*} , Benoit Montpetit ^{2,3}  and Stephen Howell ⁴ 

¹ Meteorological Research Division, Environment and Climate Change Canada, Government of Canada, Dorval, QC H9P 1J3, Canada

² Canadian Ice Service, Environment and Climate Change Canada, Government of Canada, Ottawa, ON K1A 0H3, Canada; Benoit.Montpetit2@canada.ca

³ Landscape Science and Technology Division, Environment and Climate Change Canada, Government of Canada, Ottawa, ON K1A 0H3, Canada

⁴ Climate Research Division, Environment and Climate Change Canada, Government of Canada, Toronto, ON M3H 5T4, Canada; Stephen.Howell@canada.ca

* Correspondence: Mohammed.Dabboor@canada.ca; Tel.: +1-514-421-4756

Received: 24 February 2018; Accepted: 7 April 2018; Published: 12 April 2018



Abstract: Simulated compact polarimetry from the RADARSAT Constellation Mission (RCM) is evaluated for sea ice classification. Compared to previous studies that evaluated the potential of RCM for sea ice classification, this study focuses on the High Resolution (HR) Synthetic Aperture Radar (SAR) mode of the RCM associated with a higher noise floor (Noise Equivalent Sigma Zero of -19 dB), which can prove challenging for sea ice monitoring. Twenty three Compact Polarimetric (CP) parameters were derived and analyzed for the discrimination between first year ice (FYI) and multiyear ice (MYI). The results of the RCM HR mode are compared with those previously obtained for other RCM SAR modes for possible CP consistency parameters in sea ice classification under different noise floors, spatial resolutions, and radar incidence angles. Finally, effective CP parameters were identified and used for the classification of FYI and MYI using the Random Forest (RF) classification algorithm. This study indicates that, despite the expected high noise floor of the RCM HR mode, CP SAR data from this mode are promising for the classification of FYI and MYI in dry ice winter conditions. The overall classification accuracies of CP SAR data over two test sites (96.13% and 96.84%) were found to be comparable to the accuracies obtained using Full Polarimetric (FP) SAR data (98.99% and 99.20%).

Keywords: SAR; compact polarimetry; sea ice; classification

1. Introduction

Since the inception of the RADARSAT program, Canada has been continuously providing C-band Synthetic Aperture Radar (SAR) data with the launch of RADARSAT-1 in 1995 and its successor RADARSAT-2 in 2007 [1]. The RADARSAT Constellation Mission (RCM), to be launched in late 2018, is the evolution of the RADARSAT program with the objective of ensuring data continuity, improved operational use of SAR data, and enhanced system reliability [2]. The mission, with its three identical C-band SAR satellites, will provide daily complete coverage of Canada's territory and marine regions, including the entire Arctic region [3]. The short revisit time of the mission (four days) affords a range of applications that are based on the regular collection of data and creation of composite images that highlight changes over time, such as those induced by climate change, land use evolution, coastal modifications, urban subsidence, and even human impacts on local environments [2,3]. The compact

polarimetric (CP) SAR configuration will be included in the RCM, enabling the use of CP SAR data in wide swath imagery. RCM satellites will transmit a right-circular polarization and receive two mutually coherent orthogonal (horizontal and vertical) linear polarizations (RH and RV), providing compact polarimetry as an imaging polarization option [2–5].

Operational sea ice monitoring and classification usually relies on SAR data from single- or dual-polarized beam modes, such as the ScanSAR mode of RADARSAT-2 [6–17]. However, imagery from such modes provides partial information about the radar target, which could affect the accuracy of sea ice classification. The complete information about the radar target contained in the Full Polarimetric (FP) SAR imagery can improve the sea ice classification accuracy [18–23]. However, the small image swath in the case of FP SAR data limits the operational sea ice classification to a local scale. Thus, the recently proposed CP SAR configuration for Earth observation could be a compromised choice for operational sea ice observation using SAR imagery [4,5,24]. The main advantage of such SAR systems is that they provide increased radar target information in comparison to standard dual-pol SAR systems, while covering much greater swath widths compared to FP SAR systems [24]. Such SAR architecture is already included in the current Indian Radar Imaging Satellite (RISAT-1) and the Japanese Advanced Land Observing Satellite (ALOS-2) carrying the Phased Array type L-band Synthetic Aperture Radar (PALSAR-2). The potential of CP SAR imagery for sea ice characterization is still an active research area. The first evaluation of CP SAR imagery in the ability to discriminate sea ice types and open water was reported in [24]. This evaluation was conducted visually using CP SAR data derived from FP airborne SAR images acquired over the Canadian Arctic. In [25], RISAT-1 CP SAR data was evaluated for its capability in seasonal sea ice observation over Northeastern Greenland during the melt season. A mutual information analysis was applied for the extraction of optimum CP parameters for sea ice classification. Extracted CP parameters were ingested into a trained Artificial Neural Network (ANN) classifier for sea ice classification. Results of this study showed that the first element of the Stokes vector and the Shannon entropy are useful CP parameters for sea ice classification. These results confirmed earlier findings reported in [4] using simulated CP SAR data in dry ice winter conditions. In [25], a comparison of the CP results with those obtained by spatially and temporally near-coincident RADARSAT-2 FP SAR data indicated promising results of the CP SAR configuration for sea ice observation. In another study [26], a set of CP parameters extracted from RISAT-1 CP SAR data were compared with CP parameters extracted from simulated CP SAR data obtained using near collocated RADARSAT-2 FP SAR imagery over seasonal sea ice during the melt season. This study was the first to investigate the possible effect of the non-perfectly circular RISAT-1 signal on the discrimination between sea ice types. Results of this study showed that the second element of the Stokes vector, the right co-polarized ratio and the α_s angle are three CP parameters that can be affected by a possible non-circularity of the transmitted radar signal from a CP SAR system. On the other hand, [26] found that the first element of the Stokes vector and the σ_{RH}^0 (right-circular transmit and linear horizontal receive) and σ_{RR}^0 (right-circular transmit and receive) backscattering coefficients are the best CP parameters for the separability between various sea ice types. These findings are also consistent with those reported earlier in [4] for simulated CP data, but for dry ice winter conditions. Contrary to the aforementioned studies, which are directly assessing the CP data, [27] attempted to reconstruct pseudo polarimetric covariance matrices from CP SAR data and evaluated them for sea ice classification. Herein, new reconstruction techniques for sea ice covered SAR scenes were proposed [27]. In another study [28], the reconstruction of FP information from CP SAR data was attempted considering two CP SAR configurations; the Circular Transmit and Linear Receive (CTLR) configuration and the $\pi/4$ (linear polarization oriented 45° with respect to the horizontal) configuration. The CTLR configuration was found to be suitable for the reconstruction of entropy, alpha angle, and co-polarizations, while the $\pi/4$ configuration was found to be suitable for the reconstruction of co-polarized correlation, first and second eigenvalues of the polarimetric coherency matrix, and cross-polarizations. Also, the CTLR configuration was recommended for sea ice

classification. In [29], it was found that the sea ice classification results using the m - χ decomposition technique are comparable to those obtained by the Pauli decomposition.

The RCM is planned to have ten SAR imaging modes and the compact polarization option will be available at all RCM imaging modes except for the FP SAR mode. Only two studies have investigated the potential of CP option from the different planned RCM SAR modes for sea ice monitoring and classification. The first study was conducted by [4], where simulated CP SAR data from three RCM SAR modes with different spatial resolutions (medium and low) and nominal noise floors had been evaluated for the classification of first year ice (FYI; seasonal sea ice thicker than 30 cm [6]), multiyear ice (MYI; sea ice that has survived at least one melting season [6]), and open water in dry ice winter conditions. Results showed promising performance of the tested RCM SAR modes in the discrimination of sea ice types and open water. The expected performance of the three tested RCM SAR modes in [4] was further validated in a second study in [5] using a large set of simulated RCM CP SAR data with different sea ice types, during all sea ice seasons. In [5], the effect of the radar incidence angle in the discrimination between sea ice types was also examined.

The innovative aspect of this study lies in: (1) the first evaluation of the compact polarization of the RCM High Resolution (HR) SAR mode for sea ice monitoring and (2) the performance comparison of the RCM HR mode with other RCM modes of lower spatial resolutions and noise floors. The RCM HR mode will have a nominal spatial resolution of 5 m and a nominal swath of 30 km. Although the swath of the examined mode is small, evaluation of its potential for sea ice monitoring is necessary due to its expected high Noise Equivalent Sigma Zero (NESZ) (-19 dB), compared to RCM SAR modes of medium and low spatial resolutions (NESZ from -22 dB to -25 dB). Hence, simulated CP SAR data from the RCM HR SAR mode were derived and twenty three CP parameters were extracted and evaluated for the discrimination between FYI and MYI. Histograms of FYI and MYI were created and visually interpreted and the separation between the two ice types was quantitatively estimated using the Kolmogorov-Smirnov (K-S) distance [30]. Also, the correlation between the CP parameters was analyzed by estimating the Spearman correlation coefficient values between all possible CP parameter combinations to detect possible information redundancy. Results of the RCM HR mode were compared with the results of three RCM modes we studied in [4]. These modes are the RCM Low Noise (LN; 100 m spatial resolution and -25 dB NESZ), Low Resolution (LR; 100 m spatial resolution and -22 dB NESZ), and Medium Resolution 50 m (MR50; 50 m spatial resolution and -22 dB NESZ) SAR modes. Finally, sea ice classification using a trained Random Forest (RF) classifier was performed on identified effective CP parameters of the RCM HR mode and results were evaluated and compared with classification results using FP SAR data.

2. Case Study and Environmental Conditions

The Victoria Strait and M'Clintock Channel regions in the Canadian Arctic Archipelago (CAA) were selected as study areas. The CAA is a suitable area for testing classification because of its generally wide range of ice types and negligible ice dynamics during winter [6]. Two RADARSAT-2 FP SAR images were acquired in 23 and 26 April 2015 in a descending satellite orbit direction over the Victoria Strait and M'Clintock Channel, respectively. A summary of the available SAR data is presented in Table 1. The difference in the radar incidence angle between the two images is small (1.8°) and negligible [5].

Table 1. Summary of Synthetic Aperture Radar (SAR) image acquisitions.

RADARSAT-2 Beam Mode	Acquisition Date and Time	Location	Orbit Direction	Incidence Angle	Pixel Spacing (rng \times az)
FQ21	23/04/2015 13:08:56 UTC	Victoria Strait	Descending	40.9°	4.7 m \times 5.1 m
FQ23	26/04/2015 13:21:17 UTC	M'Clintock Channel	Descending	42.7°	4.7 m \times 5.0 m

The air temperature was always below zero during the April month with a mean value of $-21.3\text{ }^{\circ}\text{C}$ according to archived Environment and Climate Change Canada weather station data from Gjoa Haven, Nunavut that is $\sim 175\text{ km}$ southeast of the study areas on King William Island. Sea ice experts from the Canadian Ice Service (CIS) identified two main ice regimes in the selected study areas: smooth thick FYI and MYI. Identifying visually main sea ice regimes by the CIS sea ice experts is usually performed using RADARSAT-2 HH and HV polarizations. This process is not difficult and does not require ground measurements. Collected sea ice regions of interest (ROIs) of the existing sea ice regimes are shown in Figure 1.

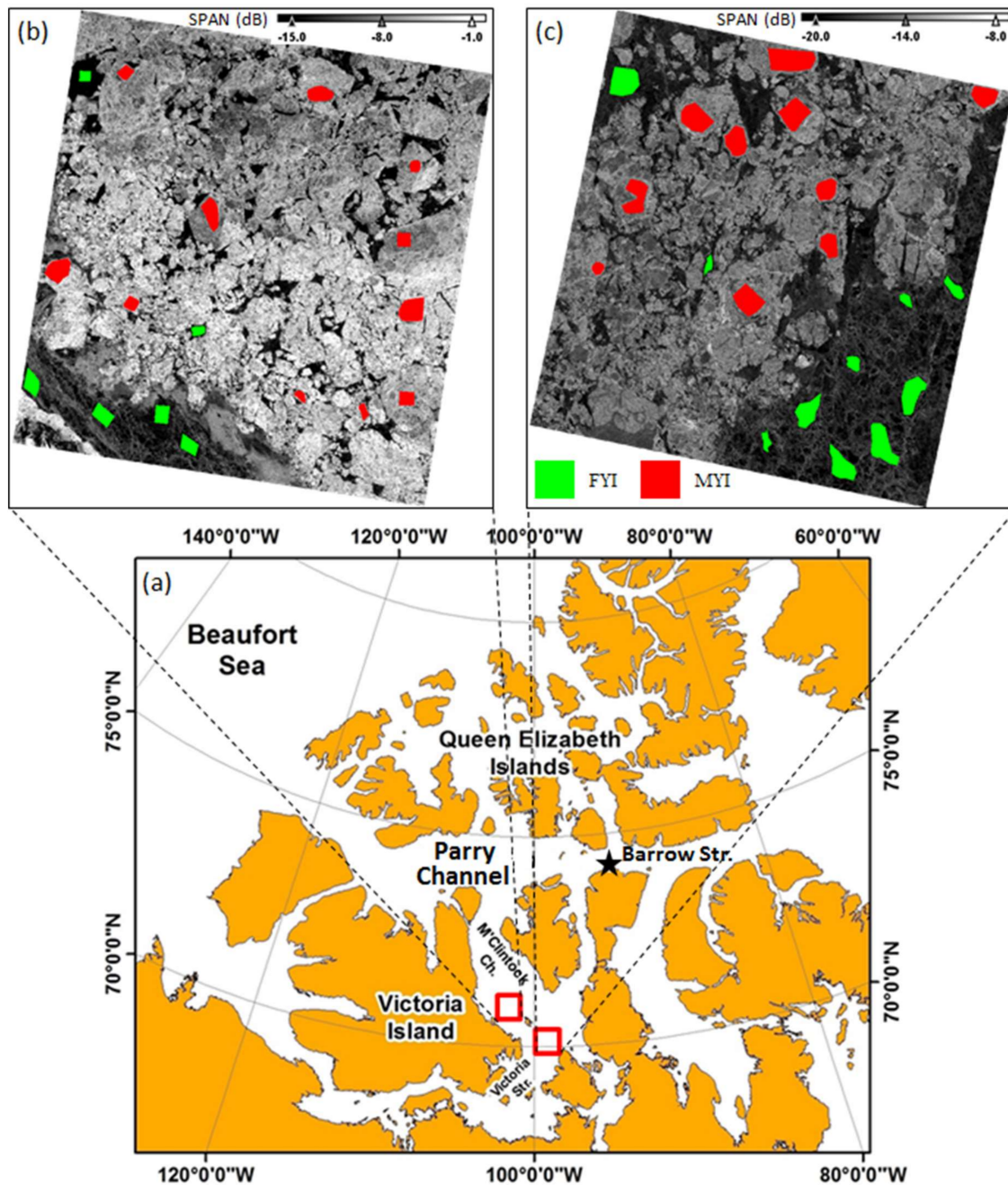


Figure 1. (a) Overview of the study areas (red rectangles) including the total backscattering power (SPAN) of the SAR images over (b) M'Clintock Channel and (c) Victoria Strait. Red polygons refer to selected multiyear ice (MYI) regions of interest (ROIs), while green polygons refer to selected first year ice (FYI) ROIs.

3. Methodology

A flowchart summarizing the followed methodology in our study is shown in Figure 2. An RCM Simulator developed at the Canada Centre for Mapping and Earth Observation [24] is used to simulate the RCM HR mode at its respective resolution (5 m) and noise floor (−19 dB). The −19 dB noise floor value represents the highest expected noise floor for the RCM HR mode. The actual noise floor value will depend on the radar beam position and the position within the beam swath. Since the swath of the RCM HR mode will be small (30 km), the range of the radar incidence angles within the swath will also be small and the change in the NESZ pattern along the swath should be minor. Following Figure 2, the RADARSAT-2 FP SAR data are ingested in the simulator to simulate the RCM CP SAR data and generate CP parameters. A refined Lee filter with a 7×7 pixel processing window is used during the simulation of the RCM CP SAR data [31]. A complete explanation of the simulator processing steps is reported in [5]. Table 2 shows the assessed CP parameters derived from the simulated RCM CP SAR data with their description. Additional information about the mathematical formulas for the calculation of each parameter can be found in [4].

Table 2. Assessed Compact Polarimetric (CP) parameters of the RADARSAT Constellation Mission (RCM) High Resolution (HR) mode.

Short Form	Description
SV0, SV1, SV2, SV3	Stokes vector elements [32]
SE_Pol, SE_Int	Shannon entropy polarimetric and intensity components [4]
$\sigma_{RL}^0, \sigma_{RR}^0, \sigma_{RH}^0, \sigma_{RV}^0$	Sigma naught backscattering—right circular transmit and left circular, right circular, linear horizontal or linear vertical receive polarization [4]
$\sigma_{RV}^0 / \sigma_{RH}^0$	Right co-polarized ratio
ρ_{RHRV}	RH RV correlation coefficient [4]
m- δ _S, m- δ _V, m- δ _DB	Surface, volume, and double bounce scattering from m- δ decomposition [24]
m- χ _odd, m- χ _V, m- χ _even	odd, volume, and even bounce scattering from m- χ decomposition [32]
m	Degree of polarization [32]
δ_{RHRV}	RH RV phase difference [24]
μ	Conformity coefficient [33]
$\sigma_{RR}^0 / \sigma_{RL}^0$	Circular polarization ratio
α_s	Alpha parameter related to the ellipticity of the compact scattered wave [34]

Histograms of FYI and MYI were calculated in each CP parameter and used for the visual interpretation of the discrimination between FYI and MYI. A quantitative analysis of the discrimination between the two ice types were followed using the Kolmogorov-Smirnov (K-S) distance [30]. The K-S distance is a nonparametric separability criterion that measures the maximum absolute difference between two cumulative distribution functions [30]. It can take values between 0 and 1. The estimation of the separability between FYI and MYI using the K-S distance leads to the identification of the CP parameters with discrimination capability between FYI and MYI (K-S distance > 0.5). The identified CP parameters can be further divided into three groups: (1) a group of some separability parameters ($0.5 < \text{K-S distance} < 0.7$); (2) a group of good separability parameters ($0.7 \leq \text{K-S distance} < 0.9$); and (3) a group of very good separability parameters ($\text{K-S distance} \geq 0.9$). The selected 0.7 and 0.9 values are reasonable threshold values to define the three aforementioned groups and were successfully used in different image processing and feature selection studies, e.g., [35–37]. A subsequent correlation analysis on the identified CP parameters with discrimination capability between FYI and MYI was conducted for possible information redundancy using the Spearman correlation coefficient (R). The Spearman correlation varies between −1 and 1 and is insensitive to outliers [38]. We assumed two CP parameters to be strongly correlated if their estimated absolute correlation value $R \geq 0.9$. CP parameters with correlation values $R < 0.9$ are assumed less correlated. We selected the threshold value of 0.9 since it was adopted and successfully used in [5,37]. The correlation analysis of the CP parameters leads to the extraction of a feature vector consisted of effective less-correlated CP parameters. Next, the

extracted feature vector was used for sea ice classification. Herein, we used the Random Forest (RF) classification algorithm, which is an ensemble machine-learning classification technique [39]. The RF classification creates rule-based classification trees by generating multiple bootstrapped samples of the original training data and creating a series of nonparametric decision trees. Each tree is grown to the largest extent possible and the classification of each object is made by simple voting of all trees [39].

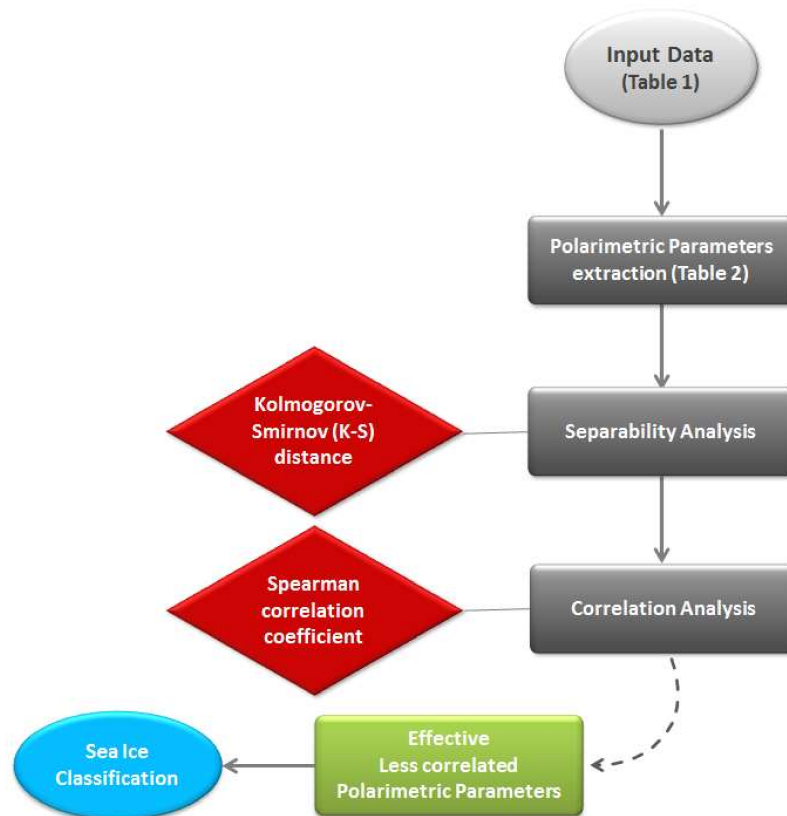


Figure 2. Methodology flowchart of the study.

4. Experimental Results

4.1. Histogram Analysis

The histograms of FYI and MYI in each simulated RCM CP parameter calculated from all the selected ROIs are shown in Figure 3. Several CP parameters appear to be promising for the discrimination between the two ice types. A visual interpretation of the histograms shows that from the elements of the Stokes vector, a separation between the FYI and MYI could be achieved using the SV0 and SV3 elements, with maximum difference between the means of FYI and MYI to be given by SV0 (0.04). We also note that this separation capability is supported by the fact that the FYI histograms in SV0 and SV3 show very small standard deviation values equal to 0.01 and 0.005 for SV0 and SV3, respectively. Furthermore, SE_Int appears to be very promising in the separation between FYI and MYI, with absolute difference between mean values equal to 2.01. Also, the four backscattering coefficients σ_{RL}^0 , σ_{RR}^0 , σ_{RV}^0 , and σ_{RH}^0 appear to be good FYI and MYI discriminators. The maximum absolute difference of mean values between FYI and MYI is obtained by the σ_{RL}^0 backscattering coefficient (5.07 dB), while the minimum absolute difference is given by the σ_{RR}^0 backscattering coefficient (2.70 dB). The histograms of σ_{RL}^0 , σ_{RR}^0 , σ_{RV}^0 , and σ_{RH}^0 in Figure 3 indicate that for smooth FYI we should expect a response at or below the nominal NESZ (−19 dB) of the RCM HR SAR mode (red vertical line in σ_{RL}^0 , σ_{RR}^0 , σ_{RV}^0 , and σ_{RH}^0 histograms), unless the NESZ is better than −19 dB. In contrary, the response from MYI in the four backscattering coefficients is expected to be higher than the nominal noise floor.

We note that in our study the σ_{RV}^0 and σ_{RH}^0 backscattering from FYI is much lower than the reported in [26]. The difference in FYI backscattering between the two studies should be related to the different environmental conditions, where in our study smooth thick FYI in dry winter conditions is investigated while in [26] wet or covered with fresh snow layer FYI was investigated during the melt season.

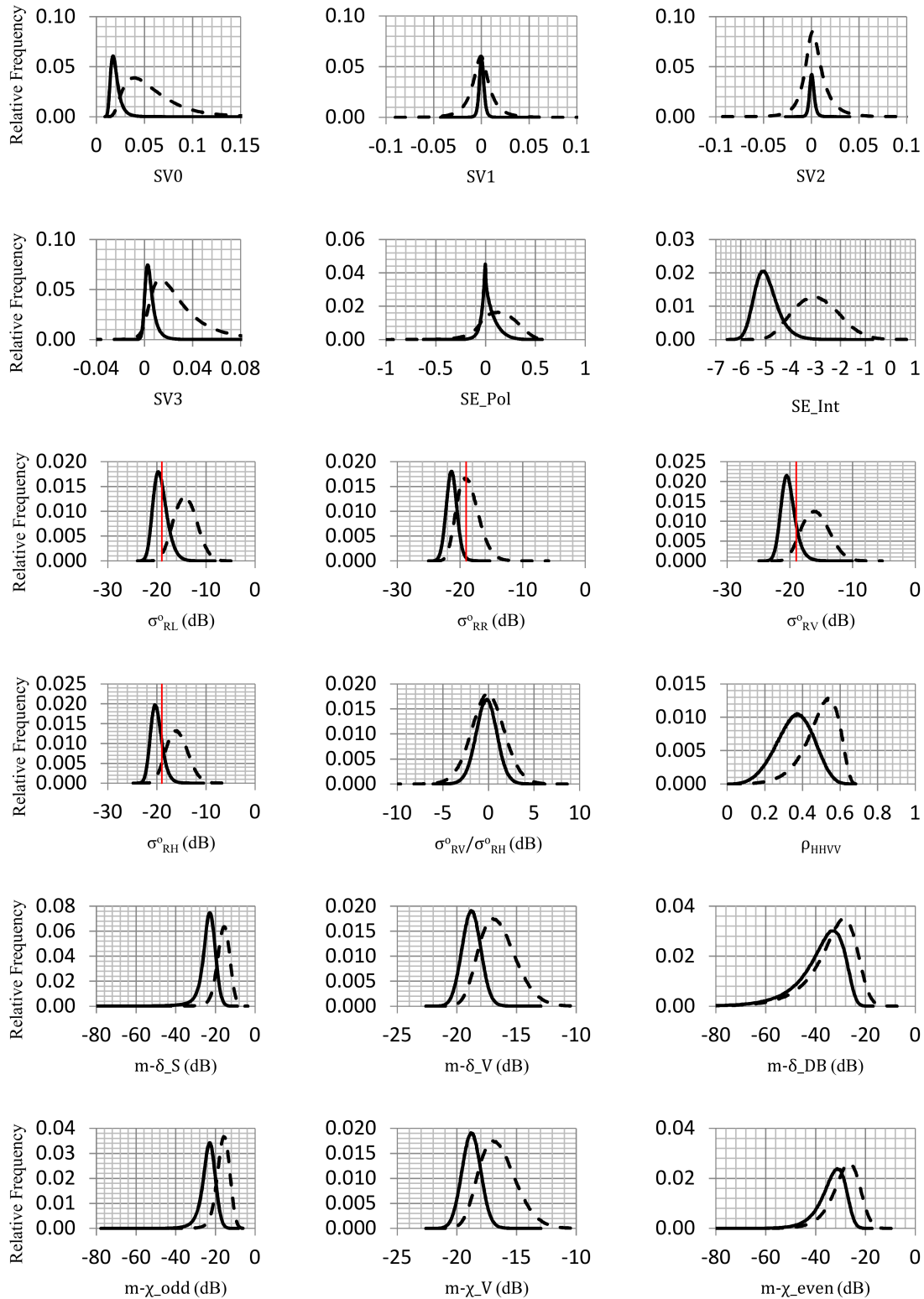


Figure 3. Cont.

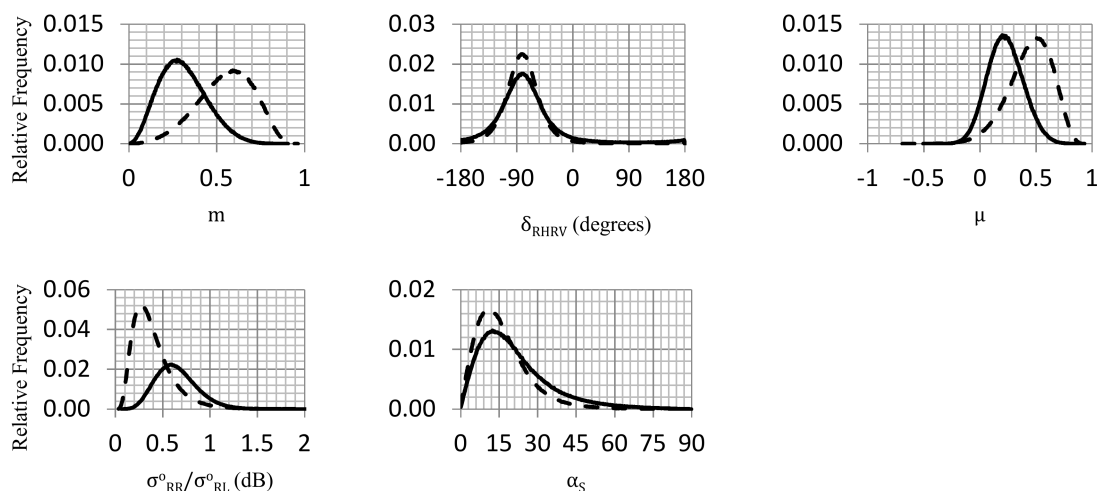


Figure 3. Histograms of CP parameters for the case of RCM HR SAR mode. Solid line refers to FYI and dashed line refers to MYI. Vertical red lines in σ_{RH}^0 , σ_{RV}^0 , σ_{RR}^0 and σ_{RL}^0 indicate a NESZ = -19 dB.

Most of the FYI and MYI histograms in the investigated CP parameters do not conform to the normal distribution (Figure 3). This suggests that the use of parametric criteria that assume the normal distribution of the sea ice types within these parameters could lead to misleading results. Thus, the analysis in the subsequent sections is conducted using nonparametric criteria, avoiding any assumptions about the statistical distributions of the two ice types.

4.2. Separability Interpretation

The discrimination between FYI and MYI in the derived CP parameters is quantitatively evaluated from the collected sea ice ROIs in Figure 1 using the K-S distance [30]. As shown in Figure 4, thirteen out of the twenty three CP parameters indicate discrimination capability between FYI and MYI (K-S distance > 0.5). Eight out of the thirteen parameters are of good separability ($0.7 \leq$ K-S distance < 0.9), while the remaining five are of some separability ($0.5 <$ K-S distance < 0.7). None of the parameters is of very good separability (K-S distance ≥ 0.9). From the four elements of the Stokes vector, SV0 (associated with the total power of the backscattered signal) and SV3 (associated with the power in the left-handed or right-handed circular polarized components) elements are detected as useful CP parameters for the discrimination between FYI and MYI (Figure 4). This is due to the fact that the returned signal from MYI is usually stronger than that from FYI in C-band SAR, because of the volume backscattering taking place due to air bubbles in MYI [6,40]. This also explains the discrimination capabilities shown by the σ_{RR}^0 backscattering coefficient (good separability) and the volume backscattering parameter from the m - δ and m - χ decompositions (some separability) [5]. The surface backscattering mechanism given by these two decomposition methods is also a useful parameter with good separability between the two ice types. In Figure 4, we also note that the backscattering coefficients σ_{RL}^0 , σ_{RV}^0 , and σ_{RH}^0 appear as parameters with good separability between FYI and MYI. These backscattering coefficients are highly correlated and behave similar to σ_{HH}^0 and σ_{VV}^0 , as reported in [5,41]. Therefore, their backscatter is expected to be low for smooth FYI and high for MYI [5,17,42]. From the Shannon entropy, only the SE_Int component show good discrimination capability between the two ice types. Some separability is also provided by the m and ρ_{RHRV} parameters. The highest contrast between FYI and MYI is given by two CP parameters; SV0 and SE_Int. Both parameters have a K-S distance equal to 0.82. The ρ_{RHRV} parameter provides the smallest K-S distance value (0.51) among the thirteen identified CP parameters. These results agree with the visual interpretation of the histograms, except for the histogram of μ which appeared to be a potential parameter for the discrimination between FYI and MYI. However, this parameter is excluded by the K-S separability criterion, where the K-S distance between the two sea ice types is equal to 0.46.

The poor discrimination capability between FYI and MYI of the μ parameter was also observed in [4,5], but for the RCM LN, LR, and MR50 modes.

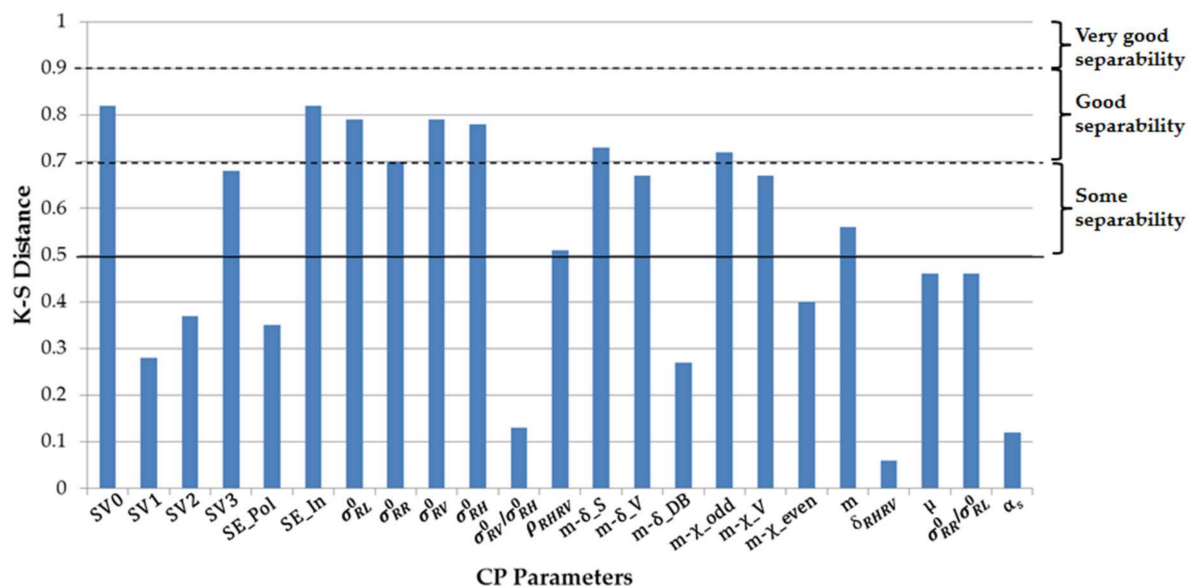


Figure 4. K-S distance between FYI and MYI in the assessed CP parameters for the RCM HR mode.

Now, we compare the results of the CP parameters from the RCM HR mode with the results of the CP parameters from the RCM LN, LR, and MR50 modes, which were investigated in [4]. In [4], a RADARSAT-2 image acquired on May 5th, 2010 over the Barrow Strait (indicated in Figure 1) in the CAA, with radar incidence angle equal to 31.2° , was used. At the image acquisition time, the air temperature was -10.4°C and the wind speed was 6.1 km/h; air temperature had been below 0°C for several months. Analytically, we compare the results of the K-S distance between FYI and MYI in the twenty three CP parameters, which we obtain in this study for the RCM HR mode with the K-S distance between the same sea ice types, but for the RCM LN, LR, and MR50 modes. FYI and MYI ROIs in [4] had been also selected by sea ice expert from the CIS. We should mention that the separability between FYI and MYI in [4] was calculated using the Jeffries–Matusita separability criterion. Thus, in order for the comparison to be fair, we had to re-estimate the separability between the two ice classes in [4] using the K-S distance.

Table 3 shows the results of the K-S distance between FYI and MYI in the four RCM modes (HR, LN, LR, and MR50). In Table 3, gray cells in each RCM mode indicate CP parameters where FYI and MYI can be separated (K-S distance > 0.5). As for the RCM HR mode, we note that for the RCM LN and LR modes thirteen out of the twenty three CP parameters present separation capability between FYI and MYI. However, for the RCM MR50 mode the number of identified parameters becomes fourteen. Furthermore, we note from Table 3 that eleven CP parameters (indicated in bold) are shared among the four RCM modes. These parameters are the SV0 and SV3 elements of the Stokes vector, SE_Int, the four backscattering coefficients σ_{RL}^0 , σ_{RR}^0 , σ_{RV}^0 , and σ_{RH}^0 , and the surface and volume backscattering mechanisms derived from the $m-\delta$ and $m-\chi$ decomposition methods. Thus, we find that these parameters remain consistent in the discrimination between FYI and MYI within the four RCM modes despite: (1) the geographic location of test sites; (2) the different nominal spatial resolutions and noise floors of the investigated four RCM modes; and (3) the difference in the radar incidence angles of the SAR images, which had an average of 10.6° . Table 3 also indicates that the CP parameters that failed to be consistent in the discrimination between the two ice types within the four RCM modes are the two (three for the RCM MR50 mode) CP parameters with the smallest K-S distance. It is worth noting that the higher noise floor of the RCM HR mode should be responsible for the decreased K-S

distance between FYI and MYI in comparison to the RCM LN, LR, and MR50 modes for eighteen out of the twenty three CP parameters (Table 3). Also, we see in Table 3 that the difference in noise floor between the RCM LN and LR modes did not change the K-S distance values between FYI and MYI in the thirteen identified CP parameters.

Table 3. K-S distance between FYI and MYI in RCM HR, LN, LR and MR50 modes. Highlighted cells in gray indicate CP parameters with K-S distance > 0.5. CP Parameters with K-S distance values in bold are parameters with discrimination capability between FYI and MYI in the four RCM modes. HR = High Resolution, LN = Low Noise, LR = Low Resolution, and MR50 = Medium Resolution 50 m.

CP Parameters	RCM HR	RCM LN	RCM LR	RCM MR50
	(5 m, −19 dB)	(100 m, −25 dB)	(100 m, −22 dB)	(50 m, −22 dB)
SV0	0.82	1.00	1.00	0.99
SV1	0.28	0.37	0.37	0.37
SV2	0.37	0.53	0.53	0.55
SV3	0.68	0.92	0.92	0.91
SE_Pol	0.35	0.49	0.29	0.26
SE_Int	0.82	1.00	1.00	0.99
σ_{RL}^0	0.79	0.98	0.98	0.97
σ_{RR}^0	0.70	1.00	1.00	1.00
σ_{RV}^0	0.79	0.99	0.99	0.98
σ_{RH}^0	0.78	0.99	0.99	0.98
$\sigma_{RV}^0/\sigma_{RH}^0$	0.13	0.18	0.20	0.18
ρ_{RHRV}	0.51	0.48	0.24	0.21
m- δ_S	0.73	0.93	0.93	0.91
m- δ_V	0.67	1.00	1.00	1.00
m- δ_{DB}	0.27	0.49	0.49	0.52
m- χ_{odd}	0.72	0.93	0.93	0.91
m- χ_V	0.67	1.00	1.00	1.00
m- χ_{even}	0.40	0.64	0.64	0.67
m	0.56	0.48	0.23	0.20
δ_{RHRV}	0.06	0.18	0.18	0.20
μ	0.46	0.49	0.27	0.23
$\sigma_{RR}^0/\sigma_{RL}^0$	0.46	0.49	0.27	0.23
α_s	0.12	0.27	0.27	0.29

4.3. Correlation Estimation

The information redundancy in the identified CP parameters with discrimination capability between FYI and MYI of the RCM HR mode is estimated using the absolute value of the Spearman correlation coefficient and shown in Figure 5.

Based on the derived Spearman correlation values (Figure 5), the thirteen identified CP parameters of the RCM HR mode are placed into groups of strongly correlated ($R \geq 0.9$) and independent (less correlated with $R < 0.9$) CP parameters (Table 4). For comparison purposes, we also applied the Spearman correlation analysis to the CP parameters of the RCM LN, LR, and MR50 modes, which we previously studied in [4] (Table 4). The CP parameters of each group in Table 4 are also sorted in a descending order in terms of their K-S distance between FYI and MYI. As shown in Table 4, the RCM HR mode has three groups of strongly correlated parameters, compared to the RCM LN, LR, and MR50 modes, which have two groups only. Also, we note in Table 4 that the RCM HR mode, in contrary to the other RCM modes, does not show any independent CP parameters. Except for m, the parameters of the first group in the RCM HR mode are shared with the second group. The rest of the CP parameters in the second group have correlation value < 0.9 with m. We note from Table 4 that the first group of strongly correlated parameters in the RCM LN, LR, and MR50 modes is identical and its parameters are included in the second group of the RCM HR mode. We see that m and ρ_{RHRV} are two parameters strongly correlated only in the case of RCM HR mode (first group in Table 4). Table 4

also shows that the strong correlation between the σ_{RR}^0 backscattering coefficient and the volume scattering mechanism (from $m\text{-}\delta$ and $m\text{-}\chi$ decompositions) is consistent within the four examined RCM modes. The results contained in Table 4 agree with those shown in Table 3 in [5].

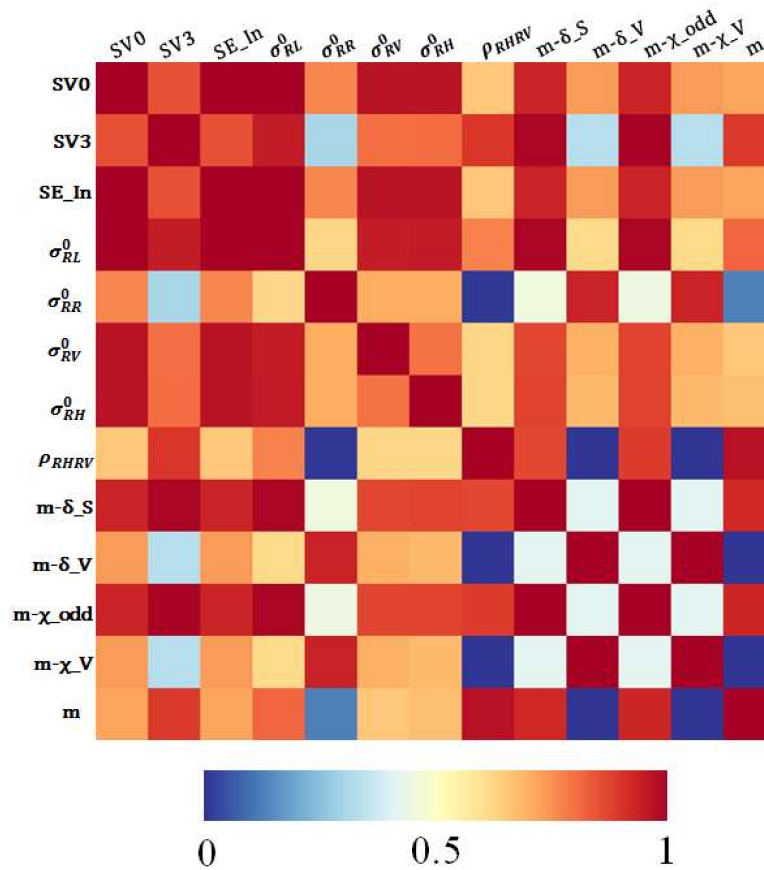


Figure 5. Absolute value of the Spearman correlation between the identified CP parameters with discrimination capability between FYI and MYI for the RCM HR mode.

A feature vector of effective polarimetric parameters is extracted for each set of polarimetric parameters. This is achieved by selecting one representative parameter from each group of strongly correlated parameters (Table 4) to form a feature vector with the independent CP parameters. We select as a representative parameter from a group of strongly correlated parameters the one with the highest K-S distance between FYI and MYI. This would be the top parameter in the sorted list of CP parameters of each group. Table 5 presents the extracted feature vectors for the four RCM SAR modes. Thus, the CP parameters of each feature vector are characterized by K-S distance between FYI and MYI > 0.5 and Spearman correlation between each other $R < 0.9$.

Table 4. Grouping of strongly correlated and independent CP parameters. HR = High Resolution, LN = Low Noise, LR = Low Resolution, and MR50 = Medium Resolution 50 m.

RCM HR			RCM LN			RCM LR			RCM MR50			
Strongly Correlated CP Parameters			Strongly Correlated CP Parameters			Independent CP Parameters	Strongly Correlated CP Parameters		Independent CP Parameters	Strongly Correlated CP Parameters		Independent CP Parameters
Group#			Group#				Group#			Group#		
1	2	3	1	2		1	2		1	2		
m- δ_S	SV0	σ_{RR}^0	SV0	σ_{RR}^0	m- χ_{even}	SV0	σ_{RR}^0	m- χ_{even}	SV0	σ_{RR}^0	m- χ_{even}	
m- χ_{odd}	SE_Int	m- δ_V	SE_Int	m- δ_V	SV2	SE_Int	m- δ_V	SV2	SE_Int	m- δ_V	SV2	
SV3	σ_{RL}^0	m- χ_V	σ_{RV}^0	m- χ_V		σ_{RV}^0	m- χ_V		σ_{RV}^0	m- χ_V	m- δ_{DB}	
m	σ_{RV}^0		σ_{RH}^0			σ_{RH}^0			σ_{RH}^0			
ρ_{RHRV}	σ_{RH}^0		σ_{RL}^0			σ_{RL}^0			σ_{RL}^0			
	m- δ_S		m- δ_S			m- δ_S			m- δ_S			
	m- χ_{odd}		m- χ_{odd}			m- χ_{odd}			m- χ_{odd}			
	SV3		SV3			SV3			SV3			
	ρ_{RHRV}											

Table 5. Extracted feature vector for each RCM SAR mode. HR = High Resolution, LN = Low Noise, LR = Low Resolution, and MR50 = Medium Resolution 50 m.

RCM HR	RCM LN	RCM LR	RCM MR50
SV0	SV0	SV0	SV0
σ_{RR}^0	σ_{RR}^0	σ_{RR}^0	σ_{RR}^0
	m- χ_{even}	m- χ_{even}	m- χ_{even}
	SV2	SV2	SV2
			m- δ_{DB}

As shown in Table 5, two CP parameters of the extracted feature vectors appear to be consistent within the four RCM modes. These parameters are the SV0 and σ_{RR}^0 backscattering coefficient. The consistency of these two parameters within the four RCM modes indicates the importance of these two CP parameters for the discrimination between FYI and MYI. This importance is confirmed by the K-S distance, where the two parameters fall in the category of good separability ($0.7 \leq$ K-S distance < 0.9) in the case of RCM HR mode and very good separability (K-S distance ≥ 0.9) in the case of RCM LN, LR and MR50 modes (Table 3). The rest of the CP parameters of the feature vectors (for the RCM LN, LR, and MR50 modes in Table 5) are not critical for the discrimination between FYI and MYI since they all fall in the category of CP parameters with some separability ($0.5 <$ K-S distance < 0.7), as shown in Table 3. The effectiveness of the SV0 and σ_{RR}^0 backscattering coefficient shown in our study for the four RCM modes is consistent with results reported in [26], which were obtained using real CP SAR data from the RISAT-1 satellite over seasonal sea ice in the melt season. The importance of the SV0 parameter for sea ice classification was also highlighted in [25] using real CP SAR data from the RISAT-1 satellite, though only seasonal sea ice during the melt season was studied.

We note the presence of the even bounce scattering mechanism from the m - χ decomposition in the RCM LN, LR, and MR50 (includes also the double bounce from the m - δ decomposition) modes as one of the parameters of the extracted feature vectors (Table 5). The presence of this scattering mechanism should have occurred occasionally in the Barrow Strait (test site in [4]), since the even or double bounce scattering mechanism did not show any discrimination capability between FYI and MYI in our current test sites (Victoria Strait and M'Clintock Channel). Finally, it is worth mentioning that the SV0 and σ_{RR}^0 parameters are directly obtained (see [4]) from the RH and RV complex polarizations, which will be the deliverables of the RCM. Thus, these parameters should be less computationally time consuming to process.

4.4. Image Classification

The extracted feature vector of the RCM HR mode is used for the classification of FYI and MYI using the RF classification algorithm. For each SAR image, half of the collected FYI and MYI ROIs were used for training the classification algorithm and the other half for estimating the classification accuracy. Figure 6a,b show the classification results for the Victoria Strait and the M'Clintock Channel test sites, respectively. The accuracies of the classification results are shown in Table 6.

High classification accuracies are obtained using the SV0 and σ_{RR}^0 backscattering coefficient as input data in the classification (Table 6). The confusion matrix shows high classification accuracies of FYI and MYI, with overall accuracy of 96.13% (Kappa = 0.916) and 96.84% (Kappa = 0.929), for Victoria Strait and M'Clintock Channel, respectively. For comparison purpose, we classified the FP SAR data over the two test sites using the RF classification algorithm. As input to the classifier, we considered the polarimetric parameters proposed in [37] for FP SAR imagery classification. These polarimetric parameters are the total backscattering power (SPAN) and the σ_{HH}^0 and σ_{HV}^0 backscattering coefficients. Figure 6 shows the classification results of the FP SAR data over Victoria Strait (Figure 6c) and M'Clintock Channel (Figure 6d). Also, classification accuracies of the FP SAR data are calculated and reported in Table 6. A visual interpretation of the classification results in Figure 6 indicates that the full polarimetric SAR provides more compact MYI floes (red) in comparison to CP SAR for both test sites. The classification results of FYI in Victoria Strait appear similar in both FP (Figure 6c) and CP (Figure 6a) SAR, while in the M'Clintock Channel the FP SAR classification of FYI (Figure 6d) appears slightly better than CP SAR (Figure 6b) especially in the bottom left FYI region. Table 6 shows that both the FP and CP SAR give high classification accuracy of FYI and MYI, with the FP SAR classification to be slightly higher than the CP SAR classification. The difference between the overall classification accuracy of FP and CP SAR is 2.86% and 2.36% for Victoria Strait and M'Clintock Channel, respectively. The classification results of the RCM HR mode in this study agree with those which we obtained in [4] for the RCM LN, LR, and MR50 modes.

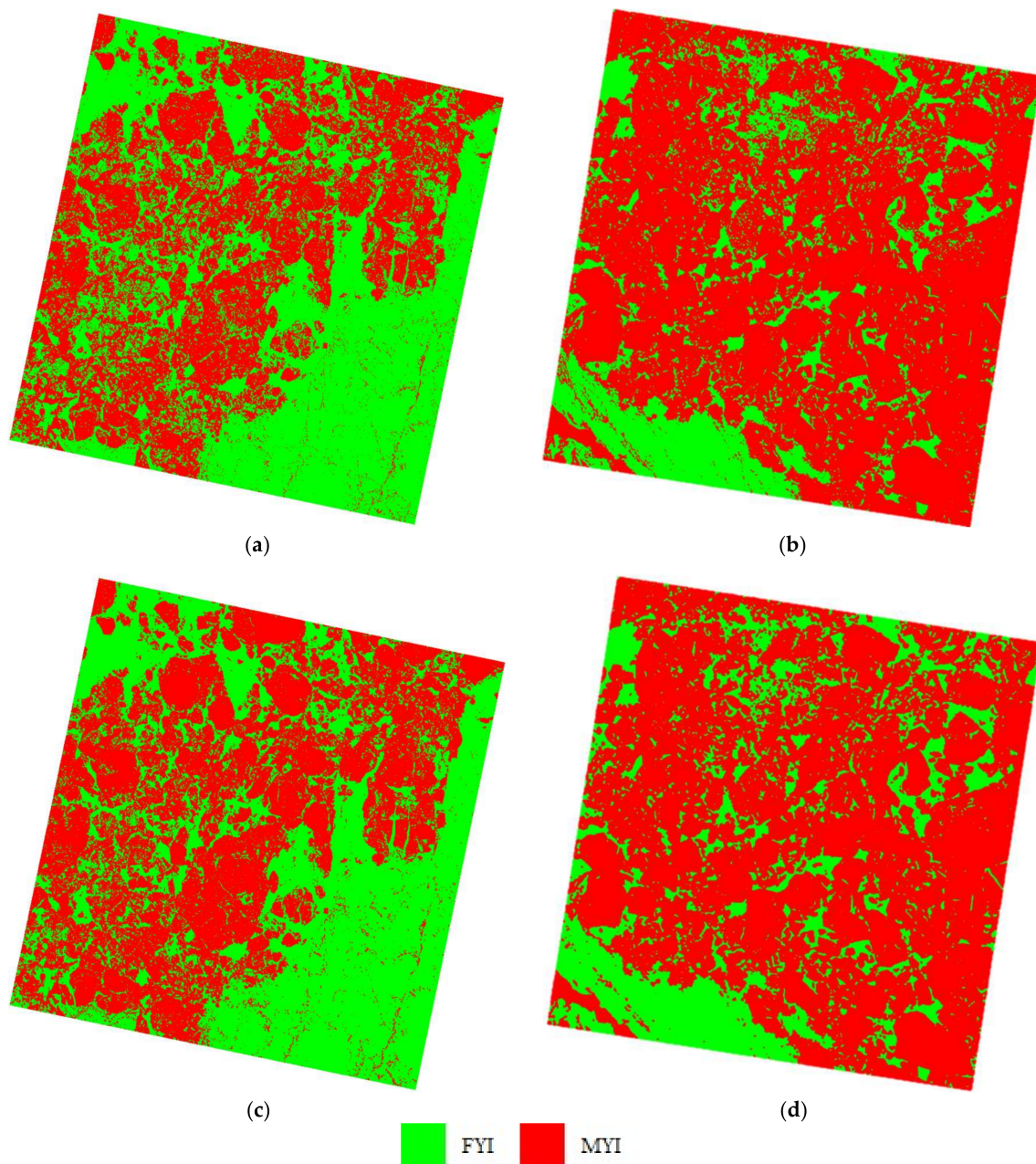


Figure 6. Classification results of the (a) Simulated RCM HR CP data over Victoria Strait; (b) Simulated RCM HR CP data over M'Clintock Channel; (c) FP SAR data over Victoria Strait; and (d) FP SAR data over M'Clintock Channel. Green color indicates FYI and red color indicates MYI.

Due to the fact that the FYI shows mean values of σ_{RR}^0 backscattering below the noise floor while the MYI shows mean values of σ_{RR}^0 backscattering slightly higher than the noise floor (Figure 3), we reapplied the RF classification using only the SV0 parameter as input. Hence, we found that the exclusion of the σ_{RR}^0 backscattering has reduced the overall classification accuracy to 91.86% for the Victoria Strait and 89.86% for the M'Clintock Channel. These reductions in the classification accuracies of FYI and MYI validated the contribution of the σ_{RR}^0 backscattering coefficient in the classification process.

Table 6. Evaluation of the FYI and MYI classification results for simulated RCM HR CP SAR data and RADARSAT-2 full polarimetric SAR data over Victoria Strait and M'Clintock Channel test sites.

		RCM HR (%)		RADARSAT-2 (%)	
		FYI	MYI	FYI	MYI
Victoria Strait	FYI	96.66	4.85	98.36	0.70
	MYI	3.34	95.15	1.64	99.30
	Overall accuracy	96.13		98.99	
	Kappa coefficient	0.916		0.977	
M'Clintock Channel	FYI	99.73	4.54	100	1.18
	MYI	0.27	95.46	0	98.82
	Overall accuracy	96.84		99.20	
	Kappa coefficient	0.929		0.982	

It is worth mentioning that several training experiments of the RF classification algorithm were conducted for the purpose of classification performance assessment. These experiments included the training of the RF classifier using some ROIs from both images (the rest were used for the validation) and the training of the RF classifier using the ROIs of one image (e.g., image over Victoria Strait) and the classification of the other as independent image (e.g., image over M'Clintock Channel). In these experiments, we found that the difference between the classification results was minor.

5. Conclusions

Analyses of twenty three CP parameters derived from simulated CP SAR data of the RCM HR mode were presented for FYI and MYI in dry ice winter conditions over two test sites in the CAA. These analyses were the first to be conducted for the RCM HR mode with its expected high noise floor in comparison to other RCM modes. A visual interpretation of the FYI and MYI histograms was conducted and followed with quantitative analysis of the separability between the two ice types and the correlation between CP parameters. Results were compared with those obtained for the RCM LN, LR and MR50 modes. This comparison is the first to be conducted between different RCM modes. This study showed that the SV0 and σ_{RR}^0 backscattering coefficient were found to be the best CP parameters for robust automated classification of FYI and MYI, not only for the RCM HR mode, but also for the RCM LN, LR, and MR50 modes. These two parameters were found consistent in their discrimination capability between FYI and MYI, despite the difference in spatial resolutions and noise floors of the RCM HR, LN, LR, and MR50 SAR modes and the difference in radar incidence angles of the used SAR imagery. Similarly to the promising sea ice classification results of the RCM LN, LR, and MR50 modes shown in [4], the RCM HR mode showed in this study encouraging automated classification results of FYI and MYI. Overall classification accuracies of FYI and MYI using the CP SAR data of the RCM HR mode (96.13% and 96.84%) were found comparable to those obtained by FP SAR data (98.99% and 99.20%). Thus, the pending arrival of CP SAR imagery from the RCM shows great promise for automated classification of main ice regimes.

Acknowledgments: Authors would like to thank Francois Charbonneau and the Canada Center for Mapping and Earth Observation for providing the RCM simulator. RADARSAT-2 data and products © MacDonald, Dettwiler and Associates Ltd. (2013)—All Rights Reserved. RADARSAT is an official mark of the Canadian Space Agency.

Author Contributions: M.D. conceived the study and processed the data. M.D., B.M. and S.H. analyzed the results. All authors contributed to the writing of the paper.

Conflicts of Interest: The authors declare no conflict of interest.

References

1. Singhroy, V.; Charbonneau, F. RADARSAT: Science and applications. *Phys. Can.* **2014**, *70*, 212–217.
2. Séguin, G.; Ahmed, S. RADARSAT constellation, project objectives and status. In Proceedings of the IEEE International Geoscience and Remote Sensing Symposium, Cape Town, South Africa, 12–17 July 2009; pp. II-894–II-897.
3. De Lisle, D.; Iris, S. RADARSAT constellation mission status update. In Proceedings of the 11th European Conference on Synthetic Aperture Radar, Hamburg, Germany, 6–9 June 2016; pp. 1–3.
4. Dabboor, M.; Geldsetzer, T. Towards sea ice classification using simulated RADARSAT constellation mission compact polarimetric SAR imagery. *Remote Sens. Environ.* **2014**, *140*, 189–195. [[CrossRef](#)]
5. Geldsetzer, T.; Arkett, M.; Zagon, T.; Charbonneau, F.; Yackel, J.; Scharien, R. All-season compact-polarimetry C-band SAR observations of sea ice. *Can. J. Remote Sens.* **2015**, *41*, 485–504. [[CrossRef](#)]
6. Shokr, M.; Sinha, N.K. *Sea Ice: Physics and Remote Sensing*; John Wiley & Sons: Hoboken, NJ, USA, 2015.
7. Casey, J.A.; Howell, S.E.; Tivy, A.; Haas, C. Separability of sea ice types from wide swath C- and L-band synthetic aperture radar imagery acquired during the melt season. *Remote Sens. Environ.* **2016**, *174*, 314–328. [[CrossRef](#)]
8. Leigh, S.; Wang, Z.; Clausi, D.A. Automated ice–water classification using dual polarization SAR satellite imagery. *IEEE Trans. Geosci. Remote Sens.* **2014**, *52*, 5529–5539. [[CrossRef](#)]
9. Zakhvatkina, N.; Korosov, A.; Muckenhuber, S.; Sandven, S.; Babiker, M. Operational algorithm for ice–water classification on dual-polarized RADARSAT-2 images. *Cryosphere* **2017**, *11*, 33–46. [[CrossRef](#)]
10. Liu, H.; Guo, H.; Zhang, L. SVM-based sea ice classification using textural features and concentration from RADARSAT-2 dual-pol ScanSAR data. *IEEE J. Sel. Top. Appl. Earth Obs. Remote Sens.* **2015**, *8*, 1601–1613. [[CrossRef](#)]
11. Wang, L.; Scott, K.A.; Clausi, D.A. Sea ice concentration estimation during freeze-up from SAR imagery using a convolutional neural network. *Remote Sens.* **2017**, *9*, 408. [[CrossRef](#)]
12. Wang, L.; Scott, K.A.; Xu, L.; Clausi, D.A. Sea ice concentration estimation during melt from dual-pol SAR scenes using deep convolutional neural networks: A case study. *IEEE Trans. Geosci. Remote Sens.* **2016**, *54*, 4524–4533. [[CrossRef](#)]
13. Johannessen, O.M.; Alexandrov, V.Y.; Frolov, I.Y.; Bobylev, L.P.; Sandven, S.; Pettersson, L.H.; Kloster, K.; Babich, N.G.; Mironov, Y.U.; Smirnov, V.G. *Remote Sensing of Sea Ice in the Northern Sea Route: Studies and Applications*; Springer-Praxis: Berlin, Germany, 2006.
14. Karvonen, J.; Simila, M.; Makynen, M. Open water detection from Baltic Sea ice Radarsat-1 SAR imagery. *IEEE Geosci. Remote Sens. Lett.* **2005**, *2*, 275–279. [[CrossRef](#)]
15. Herzfeld, U.C.; Williams, S.; Heinrichs, J.; Maslanik, J.; Sucht, S. Geostatistical and Statistical Classification of Sea-Ice Properties and Provinces from SAR Data. *Remote Sens.* **2016**, *8*, 616. [[CrossRef](#)]
16. Barber, D.G.; Yackel, J.J.; Hanesiak, J.M. Sea ice, RADARSAT-1 and arctic climate processes: A review and update. *Can. J. Remote Sens.* **2014**, *27*, 51–61. [[CrossRef](#)]
17. Geldsetzer, T.; Yackel, J. Sea ice type and open water discrimination using dual co-polarized C-band SAR. *Can. J. Remote Sens.* **2009**, *35*, 73–84. [[CrossRef](#)]
18. Dabboor, M.; Yackel, J.; Hossain, M.; Braun, A. Comparing matrix distance measures for unsupervised polarimetric SAR data classification of sea ice based on agglomerative clustering. *Int. J. Remote Sens.* **2013**, *34*, 1492–1505. [[CrossRef](#)]
19. Dabboor, M.; Shokr, M. A new Bayesian likelihood ratio test for supervised classification of fully polarimetric SAR data: An application for sea ice type mapping. *ISPRS J. Photogramm. Remote Sens.* **2013**, *84*, 1–11. [[CrossRef](#)]
20. Dabboor, M.; Howell, S.; Shokr, M.; Yackel, J. The Jeffries-Matusita separability criterion for the case of complex Wishart distribution with application to fully polarimetric SAR data. *Int. J. Remote Sens.* **2014**, *35*, 6859–6873.
21. Johansson, A.M.; King, J.A.; Doulgeris, A.P.; Gerland, S.; Singha, S.; Spreen, G.; Busche, T. Combined observations of Arctic sea ice with near-coincident collocated X-band, C-band, and L-band SAR satellite remote sensing and helicopter-borne measurements. *J. Geophys. Res. Oceans* **2017**, *122*, 669–691. [[CrossRef](#)]
22. Gill, J.; Yackel, J.J.; Geldsetzer, T. Analysis of consistency in first-year sea ice classification potential of C-band SAR polarimetric parameters. *Can. J. Remote Sens.* **2013**, *39*, 101–117. [[CrossRef](#)]

23. Moen, M.-A.N.; Doulgeris, A.P.; Anfinson, S.N.; Renner, A.H.H.; Hughes, N.; Gerland, S.; Eltoft, T. Comparison of feature based segmentation of full polarimetric SAR satellite sea ice images with manually drawn ice charts. *Cryosphere* **2013**, *7*, 1693–1705. [[CrossRef](#)]
24. Charbonneau, F.; Brian, B.; Raney, K.; McNairn, H.; Liu, C.; Vachon, P.; Shang, J.; De Abreu, R.; Champagne, C.; Merzouki, A.; et al. Compact polarimetry overview and applications assessment. *Can. J. Remote Sens.* **2010**, *36*, S298–S315. [[CrossRef](#)]
25. Singha, S.; Ressel, R. Arctic sea ice characterization using RISAT-1 compact-pol SAR imagery and feature evaluation: A case study over Northeast Greenland. *IEEE J. Sel. Top. Appl. Earth Obs. Remote Sens.* **2017**, *10*, 3504–3514. [[CrossRef](#)]
26. Espeseth, M.M.; Brekke, C.; Johansson, A.M. Assessment of RISAT-1 and Radarsat-2 for sea ice observations from a hybrid-polarity perspective. *Remote Sens.* **2017**, *9*, 1088. [[CrossRef](#)]
27. Espeseth, M.M. Synthetic Aperture Radar Compact Polarimetry for Sea Ice Surveillance. Master's Thesis, The Arctic University of Norway, Tromsø, Norway, 2015.
28. Zhang, X.; Zhang, J.; Liu, M.; Meng, J. Assessment of C-band compact polarimetry SAR for sea ice classification. *Acta Oceanol. Sin.* **2016**, *35*, 79–88. [[CrossRef](#)]
29. Li, H.; Perrie, W. Sea ice characterization and classification using hybrid polarimetry SAR. *IEEE J. Sel. Top. Appl. Earth Obs. Remote Sens.* **2016**, *9*, 4998–5010. [[CrossRef](#)]
30. Massey, F.J., Jr. The Kolmogorov-Smirnov test for goodness of fit. *J. Am. Stat. Assoc.* **1951**, *46*, 68–78. [[CrossRef](#)]
31. Lee, J.S.; Pottier, E. *Polarimetric Radar Imaging: From Basics to Applications*; CRC Press: Boca Raton, FL, USA, 2009.
32. Raney, R.K.; Cahill, J.T.S.; Patterson, G.W.; Bussey, D.B.J. The m-chi decomposition of hybrid dual-polarimetric radar data with application to lunar craters. *J. Geophys. Res.* **2012**, *117*, E00H21. [[CrossRef](#)]
33. Truong-Loi, M.; Freeman, A.; Dubois-Fernandez, P.; Pottier, E. Estimation of soil moisture and Faraday rotation from bare surfaces using compact polarimetry. *IEEE Trans. Geosci. Remote Sens.* **2009**, *47*, 3608–3615. [[CrossRef](#)]
34. Cloude, S.R.; Goodenough, D.G.; Chen, H. Compact decomposition theory. *Geosci. Remote Sens. Lett.* **2012**, *9*, 28–32. [[CrossRef](#)]
35. Ko, K.T. A Hybrid Road Identification System Using Image Processing Techniques and Back-Propagation Neural Networks. Master's Thesis, Mississippi State University, Oktibbeha County, MS, USA, 1995.
36. Desbordes, P.; Ruan, S.; Modzelewski, R.; Pineau, P.; Vauclin, S.; Gouel, P.; Michel, P.; Di Fiore, F.; Vera, P.; Gardin, I. Predictive value of initial FDG-PET features for treatment response and survival in esophageal cancer patients treated with chemo-radiation therapy using a random forest classifier. *PLoS ONE* **2017**, *12*, e0173208. [[CrossRef](#)] [[PubMed](#)]
37. Dabboor, M.; Montpetit, B.; Howell, S.; Haas, C. Improving sea ice characterization in dry ice winter conditions using polarimetric parameters from C- and L-band SAR data. *Remote Sens.* **2017**, *9*, 1270. [[CrossRef](#)]
38. Press, W.; Teukolsky, S.A.; Vetterling, W.; Flannery, B. *The Art of Scientific Computing*, 3rd ed.; Cambridge University Press: Cambridge, UK, 2007.
39. Breiman, L. Random forests. *Mach. Learn.* **2001**, *45*, 5–32. [[CrossRef](#)]
40. Mortin, J.; Howell, S.; Wang, L.; Derksen, C.; Svensson, G.; Graversen, R.G.; Schröder, T.M. Extending the QuikSCAT record of seasonal melt-freeze transitions over Arctic sea ice using ASCAT. *Remote Sens. Environ.* **2014**, *141*, 214–230. [[CrossRef](#)]
41. Geldsetzer, T.; Charbonneau, F.; Arkett, M.; Zagon, Z. Ocean wind study using simulated RCM compact-polarimetry SAR. *Can. J. Remote Sens.* **2015**, *41*, 418–430. [[CrossRef](#)]
42. Nghiem, S.V.; Bertoia, C. Study of multi-polarization C-band backscatter signatures for Arctic sea ice mapping with future satellite SAR. *Can. J. Remote Sens.* **2001**, *27*, 387–402. [[CrossRef](#)]

